I&EC research
Industrial & Engineering Chemistry Research

Article

Cite This: Ind. Eng. Chem. Res. 2018, 57, 231−241

pubs.acs.org/IECR

Microwave Solvothermal Fabrication of Zirconia Hollow Microspheres with Different Morphologies Using Pollen Templates and Their Dye Adsorption Removal

Junkai Zhao,[†] Shengsong Ge,*[,†] Lirong Liu,[†] Qian Shao,[†] Xianmin Mai,*[,‡] Cindy Xinxin Zhao,[§] Luhan Hao,[§] Tingting Wu,[∥] Zepei Yu,[†] and Zhanhu Guo*[,§]

[†]College of Chemical and Environmental Engineering, Shandong University of Science and Technology, Qingdao 266590, China

[‡]School of Urban Planning and Architecture, Southwest Minzu University, Chengdu 610041, China

[§]Integrated Composites Laboratory (ICL), Department of Chemical & Biomolecular Engineering, University of Tennessee, Knoxville, Tennessee 37996, United States

[∥]Department of Civil and Environmental Engineering, The University of Alabama in Huntsville, Huntsville, Alabama 35899, United States

ABSTRACT: Both porous and scale-like wall zirconia (ZrO_2) hollow microspheres were successfully prepared through a facile and mild microwave solvothermal method using the rape pollen as biotemplates. The formation mechanisms were discussed for both ZrO_2 hollow microspheres fabricated using pollen biotemplate with different pollen treatments. The porous ZrO_2 hollow microspheres had a specific surface area of 40.92 $m^2 \cdot g^{-1}$, significantly higher than scale-like wall ZrO_2 hollow microspheres (24.79 $m^2 \cdot g^{-1}$) and ZrO_2 particles (27.99 $m^2 \cdot g^{-1}$). The adsorption test results showed that porous ZrO_2 hollow microspheres had a higher adsorption capability (96.98 $g \cdot mg^{-1}$) than scale-like wall ZrO_2 hollow microspheres (38.55 $g \cdot mg^{-1}$) and ZrO_2 particles (32.03 $g \cdot mg^{-1}$) for Congo red. The adsorption followed pseudo-second-order kinetics, and the adsorption process was homogeneous adsorption of monolayer.

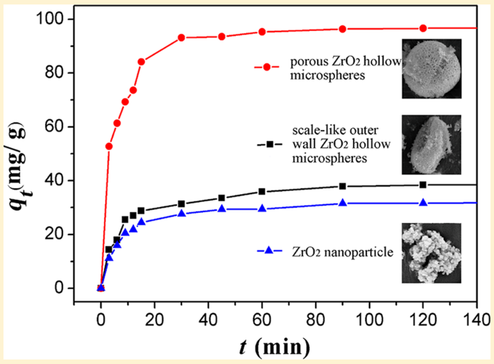

1. INTRODUCTION

The use of organic dyes becomes more and more widespread in various industries. The application of various dyes makes the environmental problems seriously, and there are still numerous problems awaited for solutions. Among the reported adsorption, photodegradation and biological methods to treat the sewage, adsorption is the most common method for treating wastewater due to its low cost and easy operation.[1−5] Zirconia (ZrO_2) is one of the most intensively studied adsorbents. For example, Tao et al. loaded aluminum oxide and zirconium oxide into montmorillonite (MMT) layers to synthesize aluminum/zirconium MMT nanocomposite adsorbents (A1MMT) and demonstrated that it could adsorb Cr^{3+} from wastewater with a capacity of 133 $mg \cdot g^{-1}$.[6] Yang et al. prepared hollow ZrO_2 microsphere by the template method and it was demonstrated to be effective on the adsorption of methyl orange and the adsorption followed the Langmuir isotherm and pseudo-second-order kinetic model.[7] Boulet et al. obtained mesoporous ZrO_2 by the sol−gel process and it had a better adsorption of CO_2, owing to their large specific surface area.[8] Particularly, the hollow ZrO_2 particles with controlled micro- and nanostructures have attracted considerable attention, owing to their low density and large surface area that contribute to their unique adsorption behavior.[9]

ZrO_2 is a promising functional material owing to its superior properties such as chemical stability, high hardness strength, excellent fracture toughness, good thermal stability, and its unique adsorption performance.[10−12] It has been extensively applied in catalysts and catalytic supports adsorption and separation, dopant of oxides for the thermoelectric power generation, metal oxide semiconductor devices, solid oxide fuel cells, etc.[13−18] Especially, hollow micro- and nanostructures have attracted considerable attentions owing to their unique structures, lower densities and larger specific surface areas.[19] The morphology has significant effects on the properties, and many available morphologies can allow property optimization for specific applications.[20] Consequently, different ZrO_2 structures, such as nanotubes, nanodots, nanowires and nanoplates that were synthesized by hydrothermal method, nanoblets and hollow fibers synthesized by template method, nanorods and spheres that were synthesized by self-assembly method, have been reported.[21−27]

The template method has been demonstrated to be very effective in synthesizing various materials without complex

Received: September 25, 2017
Revised: November 24, 2017
Accepted: December 8, 2017
Published: December 8, 2017

DOI: 10.1021/acs.iecr.7b04000

preparation. For example, carbon sphere, $CaCO_3$ cubes, butterfly wings, diatoms, yeast, and aluminum oxides have been used to synthesize different morphologies.[28−33] Compared with traditional chemical templates, the advantage of biotemplate is that it provides novel platforms on which to organize and construct chemical processes. Pollen grains, as an excellent biotemplate, have a uniform size and complex morphology and have been widely used in making various morphologies of micron/nano materials. For example, Song et al. synthesized spinous ZrO_2 core−shell microspheres with good hydrogen storage by the pollen biotemplate route.[17] Zhuang et al. obtained copper-doped TiO_2 hollow spheres using rape pollens as template and they had noticeable photocatalytic properties.[34] Recently, microwave hydrothermal method has attracted a lot of attention. Compared with the traditional hydrothermal method, microwave hydrothermal method can shorten the reaction time, avoid the agglomeration in the reaction process, and make the final morphology of the product more regular.[35,36] Therefore, more and more researches have been fosued on synthesizing various materials by microwave hydrothermal method, such as Fe-TiO_2 composite material and Co:$ZnAl_2O_4$ spinel nanoparticles.[37,38] However, ZrO_2 hollow microspheres synthesized by microwave solvothermal method using pollens as the template have not been reported yet.

In this work, rape pollen pretreated by different routes were used as biotemplates. Both porous ZrO_2 hollow microspheres and hollow ZrO_2 microspheres with scale-like outer wall were obtained by a facile, convenient and economical microwave solvothermal method. Thermogravity analysis (TGA), and Fourier transform infrared spectroscopy (FT-IR) were applied to investigate the precursors, X-ray diffraction (XRD) and X-ray photoelectron spectrometer (XPS) were used to examine the crystallinity and elemental content of the products, scanning electron microscopy (SEM) was used to characterize the morphologies of the products, nitrogen adsorption−desorption analyzer (BET) was applied to investigate the specific surface area of the as-prepared products. The adsorption performance of products was tested by the adsorption of Congo red (CR) aqueous solutions. The adsorption capacity for CR aqueous of the as-synthesized porous ZrO_2 hollow microspheres is much better compared with scale-like wall ZrO_2 hollow microspheres and ZrO_2 particles fabricated without template through the same method. The enhanced mechanism was proposed considering the unique structure and specific surface area of the sample.

2. EXPERIMENTAL SECTION

2.1. Materials.

Rape pollen was purchased from Yixing Shicheng Kanghuang Bee Industry Co. Ltd. (Yixing, China). Zirconium *n*-butoxide (80 wt %) was obtained from Shanghai Alading Reagent Co. Ltd. (Shanghai, China). Congo red (CR) was provided by Tianjin Damao Chemical Reagent Co. Ltd. (Tianjin, China). Hydrochloric acid was purchased from Chengdu Kelong Chemical Reagent Co. Ltd. (Chengdu, China). Other chemicals used were of analytical grade and used without any purification. Distilled water and absolute alcohol were used throughout.

2.2.1. Pretreatment of the Rape Pollen Template. The rape pollen grain templates for the synthesis of ZrO_2 microspheres have been prepared in two different ways. In the first method, a certain amount of fresh rape pollen was dispersed into 100 mL absolute ethanol by ultrasonication, and then the mixture was continuously stirred for 30 min. Afterward, the pollen was collected and washed with deionized water. Finally, the rape pollen was dried at room temperature. In the second method, the rape pollen was dispersed into 100 mL deionized water by ultrasonication, and then 300 mL of 8 M HCl solution was injected. Afterward, the mixture was slightly stirred for 48 h. The rape pollen was collected by extraction filtration and rinsed with a large amount of distilled water until pollen was close to neutral. Finally, the rape pollen was dried at room temperature. Two kinds of pollen templates were obtained.

2.2.2. Fabrication of ZrO_2 Microspheres. In the process of synthesis, though the templates were different, the experimental method was the same. Rape pollen (0.5 g) was dispersed into absolute ethanol (25 mL) by ultrasonication for 25 min, then zirconium-*n*-butoxide (80 wt %, 0.25 mL) was added dropwise under constant magnetic stirring. Afterward, the mixture was kept ultrasonication for 20 min, and then distilled water (0.25 mL) was injected into the mixture under the continued ultrasonication treatment. After 3 min, the mixture was transferred into the microwave reactor (XH-800S, microwave hydrothermal reactor, China). The power of the microwave reactor was set to 600 W and the system was heated to 110 °C within 15 min. After the system was treated with microwave at 110 °C for 40 min, the microwave reactor was cooled down to room temperature naturally. Then the ultimate solution was aged at room temperature for 12 h, the precipitates were filtered, washed with distilled water and absolute ethanol for several times and dried at 80 °C. Finally, the dried samples were calcined at 580 °C with a ramp rate of 1.5 °C per minute and maintaining at 580 °C for 2 h. ZrO_2 particles were fabricated through the same method but without template. The as-prepared sample (scale-like outer wall ZrO_2 hollow microspheres) using rape pollen without HCl treatment as templates was abbreviated as S-1. The sample (porous ZrO_2 hollow microspheres) made with the HCl etched rape pollen as templates, was abbreviated as S-2, and the sample (ZrO_2 particles) prepared without templates was abbreviated as S-0.

2.2.3. Adsorption Performance Experiment. The adsorption kinetic experiments were carried out by adding 10 mg of products into 30 mL of CR aqueous solution (80 $mg \cdot L^{-1}$) at room temperature (25 °C), with continuous stirring. The samples were withdrawn at fixed time intervals, and the adsorbents were separated by centrifugation at 9800 rpm for several minutes. The absorption spectrum of residual dyes was determined using UV−vis spectrophotometer (UV−vis DRS, UH4150, Hitachi, Japan) at 497 nm, corresponding to the maximum absorption wavelengths of the CR. The standard curve was made by determining the absorbance of each standard solution in order to calculate the residual CR aqueous concentrations.

The adsorption isotherm experiments were performed by adding 20 mg samples to a series of 100 mL conical flasks that contain 30 mL of CR solutions with different initial concentrations (20 to 240 $mg \cdot L^{-1}$), and the experiments were carried out at room temperature for 4 h with continuous stirring. When the adsorption reached equilibrium, the adsorbent was separated by centrifugation at 9800 rpm for 3 min, and the final concentration of CR dye in the solution was measured at maximum absorption wavelengths of Congo red (497 nm) using a UV−vis spectrophotometer.

The adsorption of CR dyes at any time (Q_t ($mg \cdot g^{-1}$)) and adsorption equilibrium (Q_e ($mg \cdot g^{-1}$)) were calculated by the following equations, respectively:[39]

$$Q_t = (C_0 - C_t)V/W \tag{1}$$

$$Q_e = (C_0 - C_e)V/W \tag{2}$$

where C_0 (mg·L^{-1}) is the initial dye concentration, C_e (mg·L^{-1}) is the equilibrium concentration, C_t (mg·L^{-1}) represents the concentrations of CR aqueous solutions at any time t, V is the volume of the CR solution (L), and W is the weight of absorbent used (g).

2.3. Characterization. The crystal structures of the products were characterized by X-ray diffractometry (XRD, ultima IV, Rigaku, Japan) using a Bruker D8-Advance diffractometer with a Cu K$_\alpha$ radiation source (λ = 0.1540 nm) at a scanning rate of 8°/min in 2θ range from 20°–80°. Fourier transform infrared (FT-IR) spectra were measured using KBr pellet on a Fourier transform infrared spectrometer (FT-IR, Nicolet 380, Thermo, America). The morphology and structural analysis of the samples were examined by scanning electron microscopy (SEM, S-4800, Hitachi, Japan). Element information on the samples was examined by an ESCALAB 250Xi X-ray photoelecton spectrometer (XPS, Thermo Scientific, USA) with an Al K$_\alpha$ X-ray source at a power of 150 W, the voltage of 15 kV, and the energy of 1486.6 eV. Thermoanalysis (TGA, Mettler, 1600HT, Switzerland) was performed at a heating rate of 15 °C min^{-1} in a dynamic atmosphere. The porous structure and surface area were analyzed by the Brunaner–Emmett–Teller (BET, Micromeritics TriStar II 3020, USA) method with N$_2$ adsorption–desorption isotherms obtained at 77.35 K using a specific surface and aperture analyzer after the samples were degassed at 180 °C. The ζ-potential was analyzed by a microiontophoresis apparatus (Powereach, JS94H, China).

3. RESULTS AND DISCUSSION

3.1. Characterization of the Products. Figure 1a shows the SEM image of pollen templates. The pollen is observed to have regular shape and it is a long narrow sphere. The length is 40–45 μm and the width is about 20 μm. Through the illustrations on Figure 1a, we can see that the pollen surface is a network structure. Figure 1b,c presents the SEM micrographs of the hollow microspheres with scaly surface (S-1). Compared with the original pollen, S-1 is similar in shape to the original pollen, but has a certain shrinkage in size. The long axis is 18–20 μm, and the short axis is 8–10 μm. The inset of Figure 1b shows a broken microsphere, indicating that the products obtained by 580 °C calcination are hollow. And a scale-liked surface was observed in Figure 1c. Figure 1d shows the pollen etched with hydrochloric acid. Under hydrochloric acid treatment, only the exine of pollen is preserved. And the pollen treated with hydrochloric acid is no longer a long narrow ellipsoid, but a nearly regular sphere and the diameter is about 20 μm. Figure 1e,f shows the porous hollow microspheres fabricated using hydrochloric acid etched pollen as templates. From Figure 1e, it can be seen that the diameter of the microspheres is about 12–14 μm and the inset of Figure 1e shows the hollow structure from a broken sphere. Furthermore, the porous surface can be clearly observed from an individual sphere in Figure 1f.

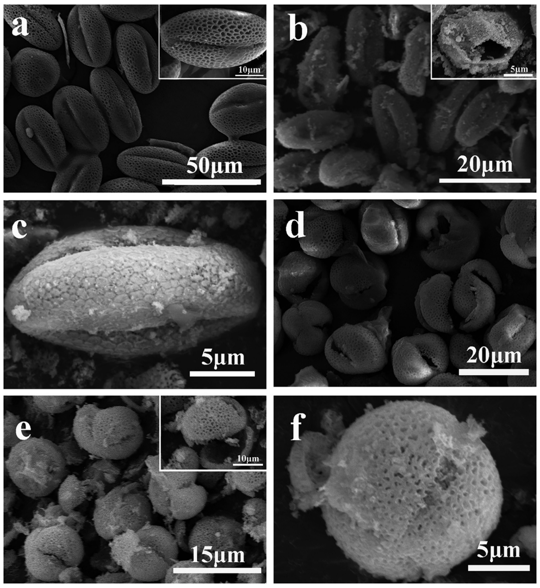

Figure 1. SEM images of rape pollen (a), S-1 (b, c), pollen etched with hydrochloric acid (d), S-2 (e, f).

The crystallinity and crystalline phase of the as-prepared samples were characterized by X-ray diffractometer (XRD), as shown in Figure 2. The XRD results show that S-0 is amorphous ZrO$_2$ before calcination, which testifies that the as-prepared samples without calcination is amorphous. However, it can be seen that S-0, S-1, and S-2 all belong to tetragonal

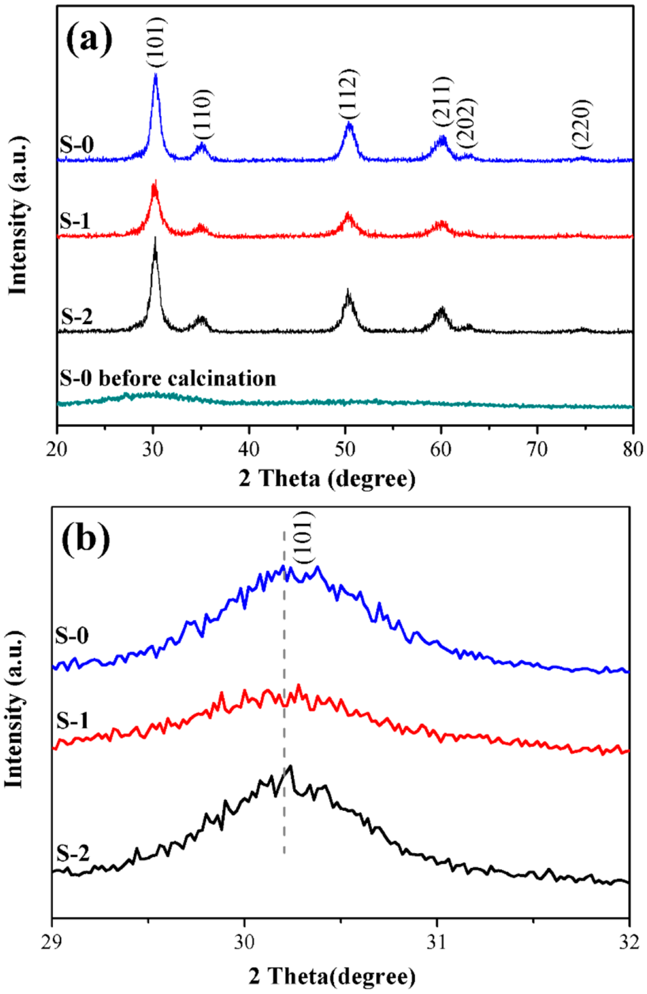

Figure 2. (a) XRD patterns of S-0, S-1, and S-2, (b) the (101) planes of S-0, S-1, and S-2 intercepted from panel a.

DOI: 10.1021/acs.iecr.7b04000
Ind. Eng. Chem. Res. 2018, 57, 231–241

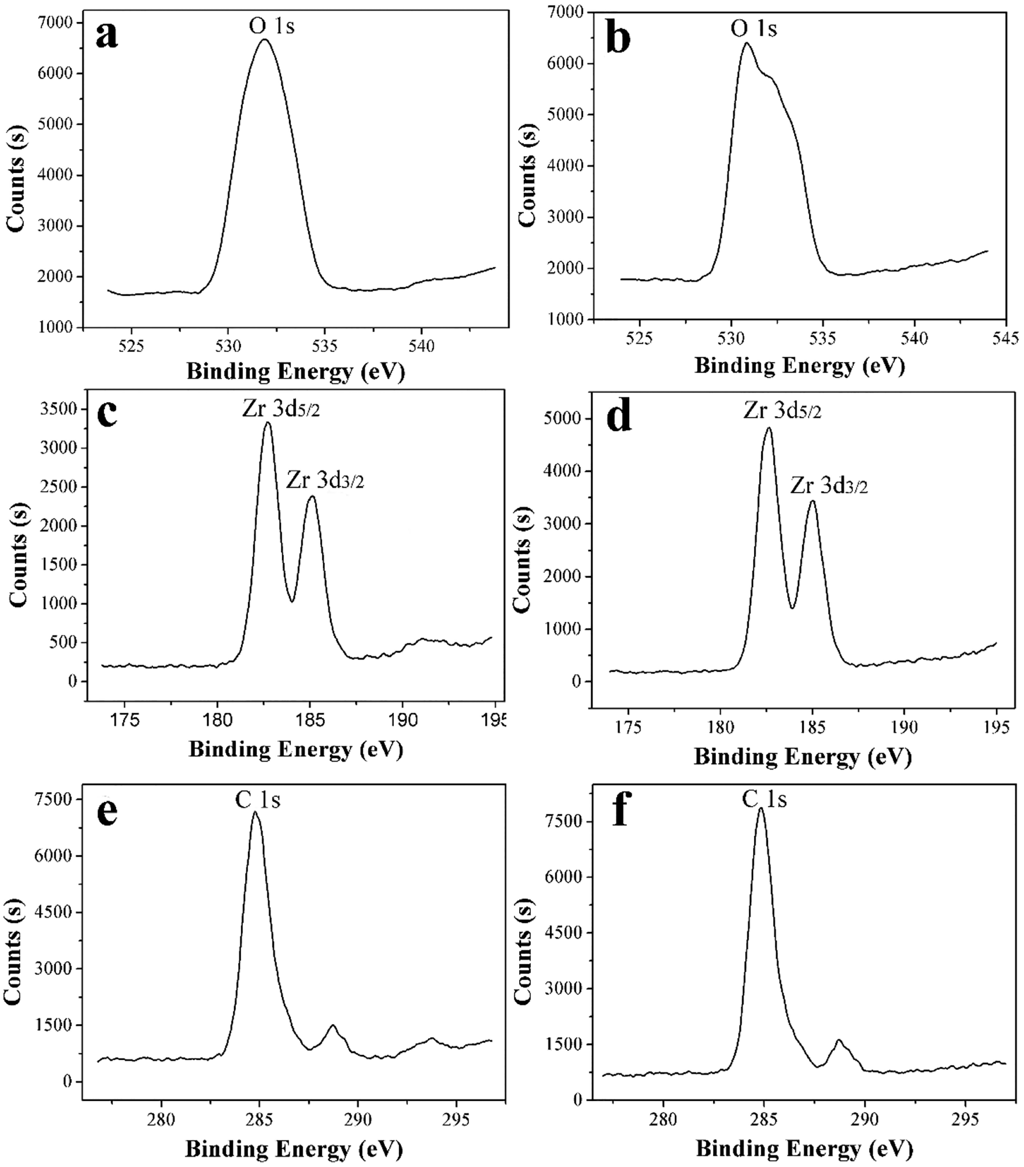

Figure 3. XPS survey spectra of S-1 (a, c, e) and S-2 (b, d, f).

crystal ZrO_2 after calcination at 580 °C (Figure 2a), and the main characteristic diffraction peaks at 2θ of 30.32°, 35.15°, 50.35°, 59.74°, 62.93°, and 74.46° can be assigned to (101), (110), (112), (211), (202), and (220) crystal planes of the tetragonal phase ZrO_2 (JCPDS card: 79-1769).[40] And from (101) crystal surface in Figure 2b and using Scherrer formula: $D_{hkl} = 0.9\lambda\ (\beta\cos\theta)^{-1}$,[41,42] the crystalline size of S-0, S-1, and S-2 is calculated to be 8.2, 8.1, and 7.4 nm, respectively. This indicates that the observed microparticles are self-assembled from small nanoparticles.

Figure 3 shows the XPS spectra of S-1 and S-2. The binding energy peaks of O 1s for S-1 and S-2 were at 529.2 eV (Figure 3a) and 531.6 eV (Figure 3b), respectively. The O 1s binding energy peak at 529.2 and 531.6 eV confirms the presence of crystal lattice oxygen (O^{2-}).[43] Figure 3c,d presents the spectra of Zr 3d for S-1 and S-2 samples. The binding energy peaks located at 183.58 and 181.08 eV can be assigned to the Zr $3d_{5/2}$ and the peaks at 185.78 and 183.48 eV are due to the Zr $3d_{3/2}$ for the Zr^{4+} state, it is proved that the product is ZrO_2.[29] Figure 3e,f indicates that both S-1 and S-2 contain trace amount of carbon element.[44] Because the biotemplate inevitably leaves carbon elements after calcination. According to the area of XPS spectrum element peak, the element mass ratio of two products can be calculated. Table 1 shows the quantity ratios of various elements in S-1 and S-2, the content of carbon in S-2 (3.6%) is much less than that in S-1 (9.2%). This is because the hydrochloric acid has removed most of the inclusions in pollen, the residue after calcination will be less. Thus, the products synthesized using pollen etched by hydrochloric acid as template have a higher purity.

Table 1. Element Content Percentage[a] of S-1 and S-2

samples	Zr (wt %)	O (wt %)	C (wt %)
S-1	67.4	23.4	9.2
S-2	71.6	24.8	3.6

[a] Element content percentage, obtained by calculating the integrated peak areas of each element in XPS spectrum.

Figure 4 shows the TGA curves of the S-1 and S-2 precursors. These two samples were heated in the temperature

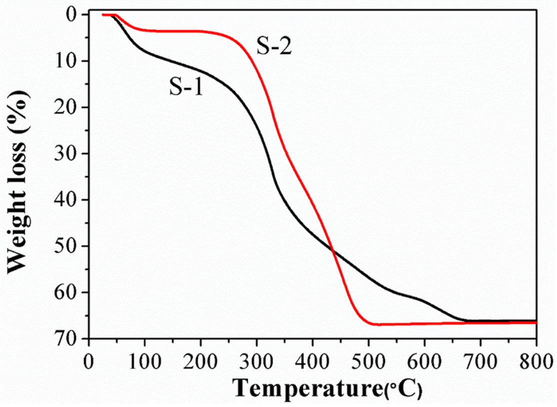

Figure 4. TGA weight loss curves of sample S-1 precursor and sample S-2 precursor.

range from room temperature to 800 °C at the heating rate of 15 °C min^{-1}. From Figure 4, both the S-1 and the S-2 have a weight loss in the temperatures range from 30 to 150 °C. The weight loss of the S-2 is due to the loss of water, the weight drops by 4.06% of the total weight, and S-1 drops by 10.85%, that is because the loss of water and other bounded water of pollen inclusions. The most obvious temperature range for weight loss is 200 to 500 °C.[34] The weight of S-1 is decreased by 44.57% of the total weight, including the decomposition of pollen walls and inclusions and the crystallization of zirconia. S-2 is decreased by 63.29% of the total weight because of the decomposition of the pollen exine and the crystallization of zirconia.[45] After 500 °C, the weight of S-2 does not change any more; however, in the temperature range of 550−680 °C, the weight of S-1 drops by 10.95% of the total weight, which is due to the decomposition of a small amount of relatively stable substances in pollen.[35] It also shows that hydrochloric acid does have a certain etching effect on pollen. The thermal measurements further confirm that most of the organic

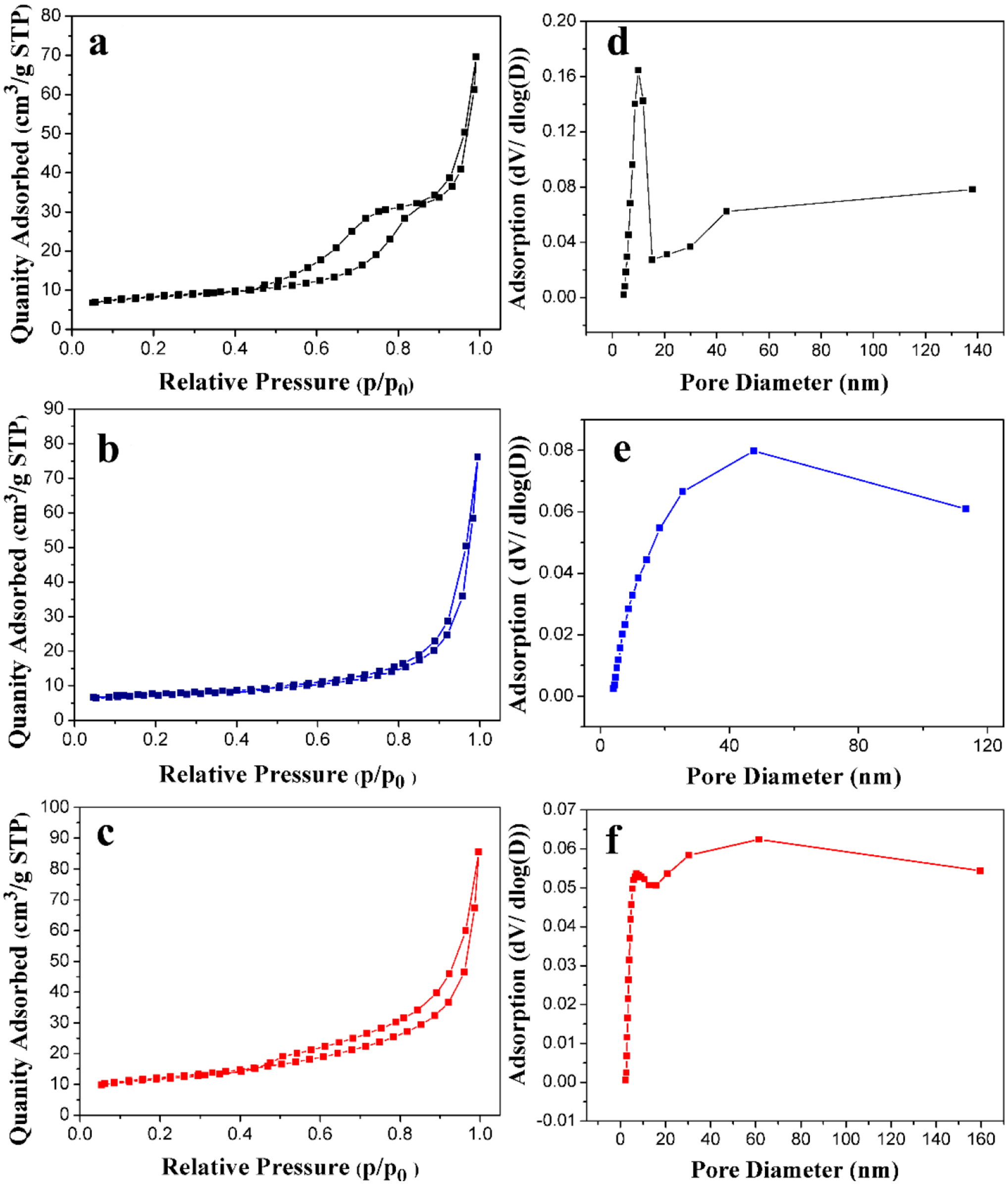

Figure 5. Nitrogen adsorption−desorption isotherms of S-0 (a), S-1 (b), and S-2 (c) and the pore size distribution of S-0 (d), S-1 (e), S-2 (f).

materials from the pollen can be removed at the experimental calcination condition of 580 °C over the designed annealing time. Meanwhile, the as-obtained samples present better crystallinity (Figure 2a) and intact hollow structure (Figure 2) even after thermal treatment at 580 °C. Based on the thermal measurements, XRD analysis and SEM images, the heat treatment was done at 580 °C

Figure 5a,b,c shows the N_2 adsorption−desorption isotherms of the products and the pore size distribution of S-0, S-1 and S-2. The BET specific surface of the samples and the relation between pore volume and diameter of S-1 and S-2 are shown in Table 2. According to the IUPAC classification, we can classify S-1 and S-2 as type III isotherms with a type H3 hysteresis loop, while type III isotherms with a type H2 hysteresis loop are more consistent with S-0.[7,46] The reason for this phenomenon may be due to the differences in templates and the accumulation of particles. Through Table 1, the specific surface areas of S-0, S-1, and S-2 are 24.79, 27.99, and 40.92 $m^2 \cdot g^{-1}$, respectively. The results indicate that the specific surface areas of S-2 is much larger than that of S-0 and S-1. That is because the S-2 is a spherical hollow structure. Although S-1 is also a hollow structure, the specific surface area difference between S-0 and S-1 is not obvious, probably because the structure of S-1 is a long and narrow sphere, the volume of the inner space is small, and the specific surface area cannot be increased effectively. From Figure 5d,e,f and Table 2, the volume of the pores for S-0, S-1, and S-2 is similar. However, the average diameter of the pores for S-0 and S-1 is 13.51 and 14.57 nm, which is obviously larger than that of S-2 (10.19 nm). In combination with an illustration of the distribution of pores in Figure 5d,e, the pore size distribution of S-2 (Figure 5f) is wider than that of S-0 and S-1.

Table 2. BET Specific Surface Areas and Pore Size of Samples S-1, S-2 and S-0[a]

sample	S_{BET} ($m^2 \cdot g^{-1}$)	V_{pore} ($cm^3 \cdot g^{-1}$)	D_{pore} (nm)
S-0	24.79	0.09	14.57
S-1	27.99	0.09	13.51
S-2	40.92	0.10	10.19

[a] BET surface area is calculated from the linear part of the BET plot (p/p_0 = 0.297). Total pore volume is taken from the volume of N_2 adsorbed at p/p_0 = 0.988. Average pore diameter is estimated using the desorption branch of the isotherm and the Barrett−Joyner−Halenda (BJH) formula.

3.2. Formation Mechanism. The FT-IR spectra of the original rape pollen and rape pollen etched with HCl are shown in Figure 6. Figure 6a indicates that there is a series of characteristic absorption peaks in the FT-IR spectrum of the rape pollen grains. The main peaks include the broad one around 3340 cm^{-1} corresponding to the stretching vibration of hydroxyl groups. The peak at 2920 cm^{-1} and the shoulder peak nearby correspond to the asymmetric stretching vibration of methylene. The inconspicuous peak at 1730 cm^{-1} indicates the vibration of carbonyl groups in lipids. The peaks at 1650 and 1480 cm^{-1} correspond to the vibration of amido I and amido II in protein, respectively. The peaks at 1050 cm^{-1} correspond to the lignin polysaccharide. And the peak at 840 cm^{-1} corresponding to the stretching vibration of hydroxyl group indicates the existence of indican.[47,48] The FT-IR spectrum of the original pollen (Figure 6a) is very similar to that of the hydrochloric acid etched pollen (Figure 6b), which indicates that the functional groups of pollen before and after hydrochloric acid treatment are basically the same. Besides, some new peaks appeared at 1120, 1260, and 830 cm^{-1} as shown in Figure 6c,d, which correspond to the asymmetric stretching vibration and asymmetric stretching vibration of R−Zr−O and Zr−O−Zr.[49] The peaks at 1730 cm^{-1} become weakened, this may be due to the interactions of these functional groups and Zr(IV). And the peaks at 1650 and 830 cm^{-1} disappeared, which is perhaps induced by the chemical bonds between the functional groups and the Zr(IV). This shows that two kinds of rape pollen have played a certain induction effect as a template.[50]

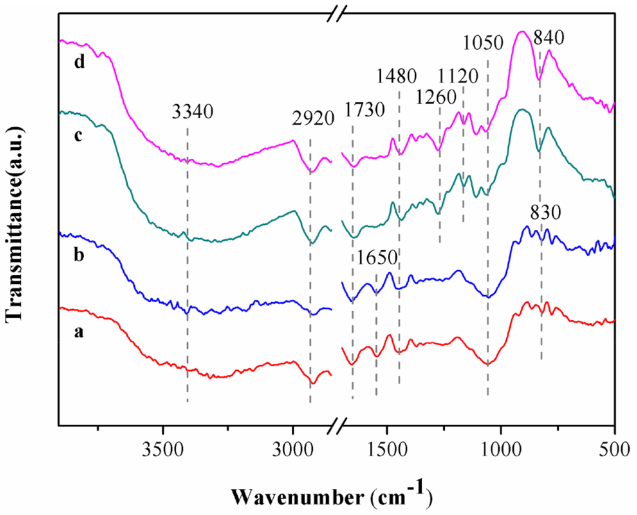

Figure 6. FT-IR of the rape pollen (a), pollen etched with HCl (b), S-1 before calcination (c), and S-2 before calcination (d).

The possible formation of S-1 and S-2 samples is shown in Figure 7. First of all, we can come to a conclusion that the pollen wall has two layers, after hydrochloric acid etching, the pollen intine and other inclusion were decomposed and then issued from the pore canals of the pollen wall.[51] Therefore, pollen only retained pollen wall after being treated with hydrochloric acid. Because of the pollen is different before and after treatment, the formation mechanism will show disparity. Figure 7a illustrates that the preparation of S-1 can be summarized as three steps. In the first step, zirconium *n*-butoxide was converted into small droplets under ultrasonic treatment, went through the pores of the pollen wall, and accumulated between the two layers of pollen wall. At the same time, abundant functional groups on the pollen wall produce an electrostatic force to attract zirconium *n*-butoxide molecule to be adsorbed on the pollen wall. The adsorption process of zirconium *n*-butoxide onto pollen wall is schematically shown in Figure 7c. In the second step, the adsorbed zirconium *n*-butoxide on pollen walls was hydrolyzed to amorphous ZrO_2 under the microwave thermal treatment (Figure 2a). Finally, during calcination, the template is removed and ZrO_2/pollen core−shell microspheres is converted to scale-like wall ZrO_2 Hollow spheres. As for S-2, the process is similar to the process of making S-1. The difference is in the first step, small drops of zirconium *n*-butoxide are only attached to the outer and inner surfaces of the pollen exine, instead of accumulating between two walls. The zirconium *n*-butoxide molecules are adsorbed onto pollen outer walls that contain a large number of functional groups. Subsequently, zirconium *n*-butoxide was also hydrolyzed to ZrO_2 under microwave thermal treatment.

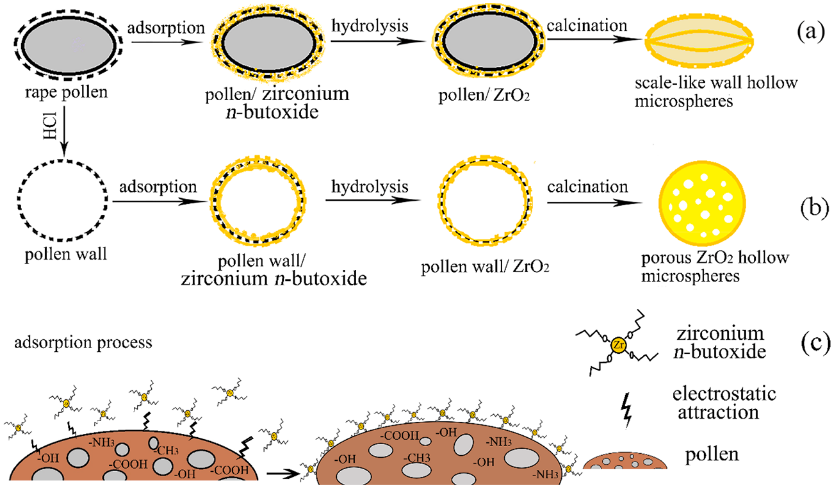

Figure 7. Schematic illustration of scale-like wall ZrO_2 hollow spheres (a), porous ZrO_2 hollow microspheres (b), and adsorption process of S-1 and S-2 (c).

Finally, with increasing the calcination temperature, the template is gradually removed, porous ZrO_2 hollow microspheres are fabricated.

3.3. Adsorption Performance. The adsorption kinetic studies of S-0, S-1, and S-2 are shown in Figure 8. Figure 8a shows that the adsorption of all samples increases remarkably during the first 30 min and then increases at a relatively slow rate, and the final equilibrium is achieved within ∼120 min. In addition, although the crystal type is the same, the adsorption capacities of the three products demonstrated large differences. The equilibrium adsorption capability values of S-0, S-1, and S-2 are 32.03, 38.55, and 96.98 $mg \cdot g^{-1}$, respectively. The results indicate that S-2 exhibits much better adsorption performance than S-0 and S-1, which is due to the larger specific surface area and more pore volume of S-2.

In this study, pseudo-first-order and pseudo-second-order kinetic models were used to investigate the adsorption kinetics of these three samples. The pseudo-first-order and pseudo-second-order rate equations are expressed as follows:[52]

$$\ln(Q_e - Q_t) = \ln(Q_e - K_1 t) \tag{3}$$

$$\frac{t}{Q_t} = \frac{1}{K_2 Q_e^2} + \frac{t}{Q_e} \tag{4}$$

where Q_t represents the adsroption of CR dyes at any time t, and Q_e is the adsorption of CR dyes at adsorption equilibrium, K_1 (min^{-1}) and K_2 ($g(mg^{-1} \cdot min^{-1})$) are pseudo-first-order rate constant and pseudo-second-order rate constant, respectively.

Table 3 displays the correlation coefficients (R^2) and adsorption kinetic constants of the pseudo-first-order and pseudo-second-order models. The values of slope (K_1 and K_2) are calculated from Figure 8b,c, respectively. Based on the values of Q_e calculated by the above two adsorption kinetics models, it is obvious that the Q_e calculated by the pseudo-second-order model fits better with the experimental values. Moreover, the R^2 of three samples was obtained by pseudo-second-order model are greater than 0.99. Therefore, the pseudo-second-order model is more suitable for describing the adsorption kinetics of CR dye using these three samples as adsorbents.

By measuring the ζ-potential on the surface of ZrO_2 (S-2), it is found that the surface of ZrO_2 has a positive charge (ζ-

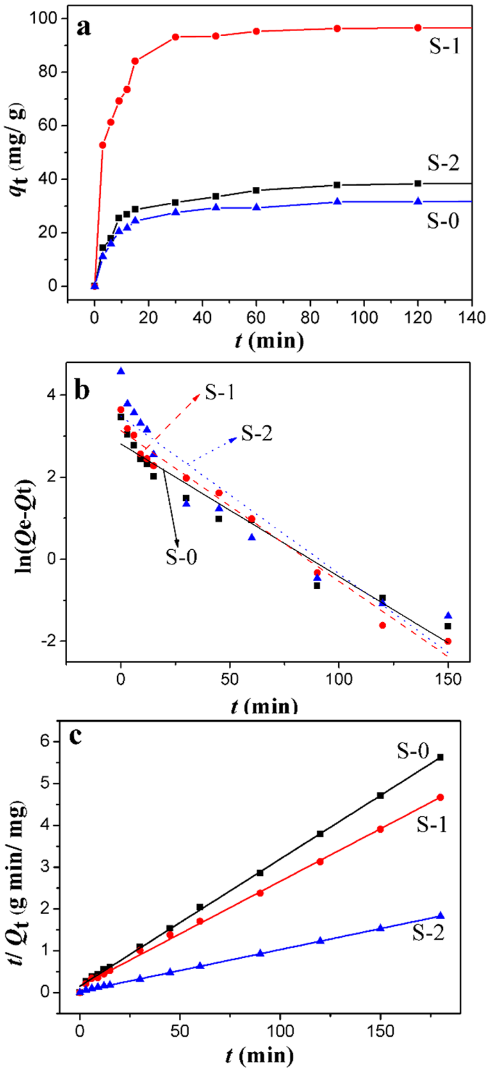

Figure 8. Adsorption kinetics for CR adsorption on S-1, S-2, and S-0 (a); pseudo-first-order kinetics isotherms for CR adsorption on S-0, S-1, and S-2 (b); pseudo-second-order kinetics isotherms for CR adsorption on S-0, S-1, and S-2 (c).

Table 3. Pseudo-First-Order Kinetics and the Pseudo-Second-Order Kinetics Isotherm Constants of CR Adsorption on S-0, S-1 and S-2[a]

	experimental values	pseudo-first-order kinetics			pseudo-second-order kinetics		
samples	Q_e (mg·g^{-1})	Q_e (mg·g^{-1})	K_1 (min^{-1})	R^2	Q_e (mg·g^{-1})	K_2 (g (mg^{-1}·min^{-1}))	R^2
S-0	32.03	16.67	0.03235	0.948	32.90	0.00633	0.999
S-1	38.55	23.05	0.03675	0.976	39.74	0.00451	0.998
S-2	96.98	32.77	0.03839	0.894	98.13	0.00378	0.999

[a] Experimental data is obtained by kinetic adsorption experiment: adsorbent (20 mg) was stirred for 2 h in Congo red solution (30 mL, 80 mg/L) at room temperature to achieve the adsorption equilibrium.

potential = 55.695 mV), i.e., ZrO_2 carries stronger positive charges on its surface. The ionization reaction of Congo red dye in aqueous solution is as follows:

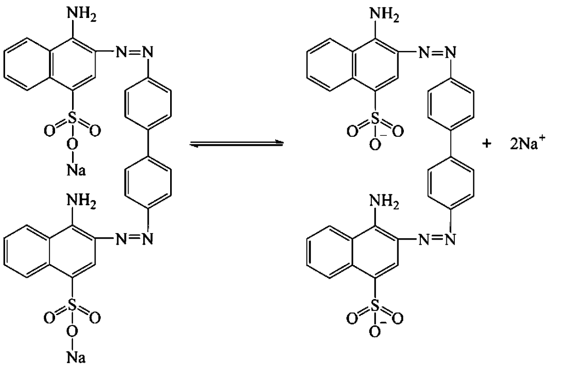

(5)

Therefore, Congo red is present in aqueous solution in the form of negative ions. Due to the existence of attractive electrostatic forces between the positively charged porous ZrO_2 hollow microsphere surface and the negatively charged Congo red molecules, Congo red molecules are firmly adsorbed on the surface of porous ZrO_2 hollow microspheres.[53] The mechanism of adsorption is shown in Figure 9. This can also be confirmed by the decrease of the ζ-potential of ZrO_2 (39.471 mV) after the adsorption of Congo red molecule. The experimental data of adsorption kinetics and the change of ζ-potential value on the ZrO_2 surface show that the adsorption of Congo red on ZrO_2 is mainly a chemical adsorption process, which is consistent with the observations in other systems.[54,55]

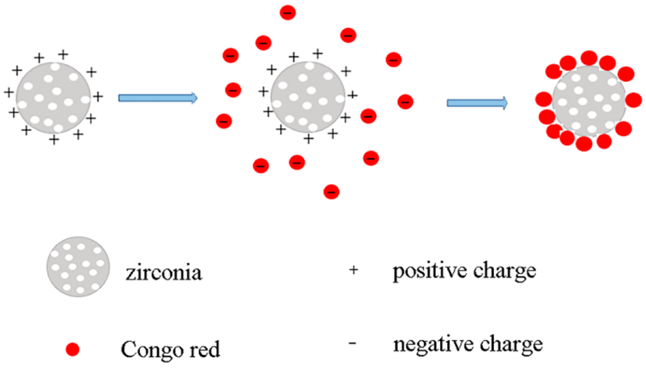

Figure 9. Schematic illustration of adsorption mechanism of ZrO_2 on Congo red.

Figure 10 shows the adsorption isotherms of S-0, S-1, and S-2. The maximum adsorption capacity of the three samples is observed to increase gradually with the increase of the concentration of Congo red dye. Finally, three samples reached the maximum equilibrium adsorption, and the maximum adsorption values of S-0, S-1, and S-2 are 33.09, 39.62, and 97.37 mg·g^{-1}, respectively.

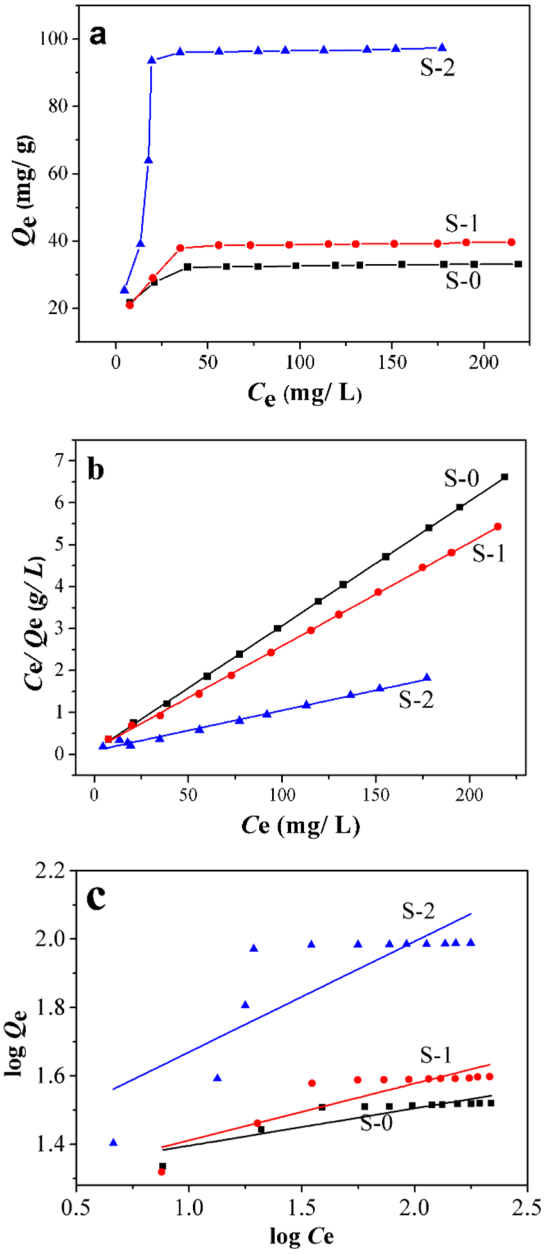

Figure 10. Adsorption isotherms for CR adsorption on S-0, S-1, and S-2 (a); Langmuir isotherms for CR adsorption on S-0, S-1, and S-2 (b); Freundlich isotherms for CR adsorption on S-0, S-1, and S-2 (c).

The Langmuir equation and Freundlich equation were used to describe the adsorption process and analyze the experimental

Table 4. Langmuir and Freundlich Isotherm Constants of S-0, S-1, and S-2[a]

	experimental values	Langmuir isotherm model			Freundlich isotherm model		
samples	Q_m ($mg\cdot g^{-1}$)	Q_m ($mg\cdot g^{-1}$)	K_L ($L\cdot mg^{-1}$)	R^2	n ($mg^{(1-(1/n))}\cdot L^{(1/n)}\cdot g^{-1}$)	K_F ($mg^{(1-(1/n))}\cdot L^{(1/n)}\cdot g^{-1}$)	R^2
S-0	33.09	32.61	0.3122	0.999	9.1533	19.3615	0.764
S-1	39.62	38.75	0.2072	0.999	6.0176	17.6068	0.745
S-2	97.37	92.68	0.1115	0.991	3.0938	22.2254	0.666

[a] Experimental values are obtained by kinetic adsorption experiment: adsorbent (20 to 240 mg) was stirred for 2 h in Congo red solution (30 mL, 80 mg/L) at room temperature to achieve adsorption equilibrium.

data in this study. The Langmuir isotherm and Freundlich isotherm equations are expressed as follows:[56,57]

$$\frac{C_e}{Q_e} = \frac{1}{K_L Q_m} + \frac{C_e}{Q_m} \tag{6}$$

$$\log Q_e = \log K_F + \frac{1}{n}\log C_e \tag{7}$$

where Q_m ($mg\cdot g^{-1}$) represents the maximum adsorption capacity, K_L ($L\cdot mg^{-1}$) and K_F ($mg^{(1-(n-1))}\cdot L^{(n-1)}\cdot g^{-1}$) are the Langmuir and Freundlich constants, respectively, and n ($g^{(1-(1/n))}\cdot L^{(1/n)}\cdot g^{-1}$) is the heterogeneity factor.

Table 4 shows the fitting results for the adsorption capacity of S-0, S-1, and S-2. The Langmuir and Freundlich constants were calculated from the plots in Figure 10b,c. It can be observed that the Langmuir theoretical Q_m values are close to the experimental values of Q_m. Based on the Langmuir model having a higher R^2 compared with Freundlich model, the adsorption isotherms were fitted more accurately by the Langmuir equation. Therefore, the adsorption process is more suitable to be described by the Langmuir model. It shows that the adsorption process is homogeneous adsorption of monolayer.[58]

4. CONCLUSIONS

In summary, ZrO_2 hollow microspheres with both scaly surface and porous structures were successfully synthesized by microwave solvothermal method. The difference in template processing is the main reason for obtaining microspheres with different morphologies. The porous ZrO_2 hollow microspheres prepared using pollen etched with HCl demonstrated a higher adsorption (96.98 $mg\cdot g^{-1}$) than scale-like wall ZrO_2 hollow microspheres (38.55 $mg\cdot g^{-1}$) and ZrO_2 particles (32.03 $mg\cdot g^{-1}$). The adsorption isotherms of samples are better described by Langmuir isotherm equation and the adsorption process follows the pseudo-second-order kinetic model. The adsorption type is a chemical process. The above results show that porous ZrO_2 hollow microspheres synthesized by microwave solvothermal method using pollen as templates have excellent adsorption properties and potential applications in the removal of organic dyes from polluted wastewater.

■ AUTHOR INFORMATION

Corresponding Authors

*Email: geshengsong@126.com (S.G.).
*Email: aixianmin@foxmail.com (X.M.).
*Email: zguo10@utk.edu (Z.G.).

ORCID

Zhanhu Guo: 0000-0003-0134-0210

Notes

The authors declare no competing financial interest.

■ REFERENCES

(1) Shi, H.; Li, W.; Zhong, L.; Xu, C. Methylene Blue Adsorption from Aqueous Solution by Magnetic Cellulose/Graphene Oxide Composite: Equilibrium, Kinetics, and Thermodynamics. *Ind. Eng. Chem. Res.* **2014**, *53*, 1108.

(2) Xiang, X.; Pan, F.; Li, Y. A review on adsorption-enhanced photoreduction of carbon dioxide by nanocomposite materials. *Adv. Compos. Hybrid Mater.* **2017**, in press, DOI: 10.1007/s42114-017-0001-6.

(3) Ma, Y. L.; Lv, L.; Guo, Y. R.; Fu, Y. J.; Shao, Q.; Wu, T. T.; Guo, S. J.; Sun, K.; Guo, X. K.; Wujcik, E. K.; Guo, Z. H. Porous lignin based poly (acrylic acid)/organo-montmorillonite nanocomposites: swelling behaviors and rapid removal of Pb (II) ions. *Polymer* **2017**, *128*, 12.

(4) Wang, Z. X.; Yang, X. B.; Cheng, Z. J.; Liu, Y. Y.; Shao, L.; Jiang, L. Simply Realizing "Water Diode" Janus Membranes for Multifunctional Smart Applications. *Mater. Horiz.* **2017**, *4*, 701.

(5) Zhang, Y. Q.; Yang, X. B.; Wang, Z. X.; Long, J.; Shao, L. Designing multifunctional 3D magnetic foam for effective insoluble oil separation and rapid selective dye removal for use in wastewater remediation. *J. Mater. Chem. A* **2017**, *5*, 7316.

(6) Tao, E.; Ma, H. R.; Li, Y. A cleaner Al_2O_2-ZrO_2/mmt nanocomposite adsorbent based on Al-Zr tanning waste. *J. Am. Leather Chem. Assoc.* **2014**, *109*, 389.

(7) Yang, X.; Song, X.; Wei, W.; Wei, Y.; Hou, L.; Fan, X. Synthesis of hollow ZrO_2 mesopores microspheres with strong adsorption capability by the yeast bio-template route. *J. Nanosci. Nanotechnol.* **2011**, *11*, 4056.

(8) Boulet, P.; Knöfel, C.; Kuchta, B.; Hornebecq, V.; Llewellyn, P. L. Computational investigation of the adsorption of carbon dioxide onto zirconium oxide clusters. *J. Mol. Model.* **2012**, *18*, 4819.

(9) Hu, J.; Chen, M.; Fang, M.; Wu, L. Fabrication and application of inorganic hollow spheres. *Chem. Soc. Rev.* **2011**, *40*, 5472.

(10) Liu, X.; Kan, C.; Wang, X.; Yang, X.; Lu, L. Self-assembled nanodisks with targetlike multirings aggregated at the air–water interface. *J. Am. Chem. Soc.* **2006**, *128*, 430.

(11) Jiang, X.; Li, S. W.; Shao, L. Pushing CO_2-philic membrane performance to the limit by designing semi-interpenetrating networks for sustainable CO_2 separations. *Energy Environ. Sci.* **2017**, *10*, 1339.

(12) Chen, S. Y.; Jang, L. Y.; Cheng, S. Synthesis of thermally stable zirconia-based mesoporous materials via a facile post-treatment. *J. Phys. Chem. B* **2006**, *110*, 11761.

(13) Wu, T. H.; Shao, Q.; Ge, S. S.; Liu, Q. Y.; Zhao, W. Influence of molecular weight of chitosan on the microstructures and photocatalytic property of ZrO_2 prepared by chitosan templates method. *Mater. Res. Bull.* **2016**, *83*, 657.

(14) Badoga, S.; Dalai, A. K.; Adjaye, J.; Hu, Y. Combined effects of EDTA and heteroatoms (Ti, Zr, and Al) on catalytic activity of SBA-15 supported NiMo catalyst for hydrotreating of heavy gas oil. *Ind. Eng. Chem. Res.* **2014**, *53*, 2137.

(15) Ahmed, A. I.; El-Hakam, S. A.; Samra, S. E.; El-Khouly, A. A.; Khder, A. S. Structural characterization of sulfated zirconia and their catalytic activity in dehydration of ethanol. *Colloids Surf., A* **2008**, *317*, 62.

(16) Feng, Y.; Jiang, X.; Ghafari, E.; Kucukgok, B.; Zhang, C.; Ferguson, I.; Lu, N. Metal oxides for thermoelectric power generation and beyond. *Adv. Compos. Hybrid Mater.* **2017**, in press, DOI: 10.1007/s42114-017-0011-4.

(17) Hsu, D. C.; Wang, M. T.; Lee, J. Y.; Juan, P. C. Electrical characteristics and reliability properties of metal-oxide-semiconductor field-effect transistors with ZrO_2 gate dielectric. *J. Appl. Phys.* **2007**, *101*, 094105.

(18) Kumari, L.; Li, W. Z.; Xu, J. M.; Leblanc, R. M.; Wang, D. Z.; Li, Y.; Guo, H.; Zhang, J. Controlled hydrothermal synthesis of zirconium oxide nanostructures and their optical properties. *Cryst. Growth Des.* **2009**, *9*, 3874.

(19) Huang, J. N.; Cao, Y. H.; Shao, Q.; Peng, X. F.; Guo, Z. H. Magnetic nanocarbon adsorbents with enhanced hexavalent chromium removal: morphology dependence of fibrillar vs particulate structures. *Ind. Eng. Chem. Res.* **2017**, *56*, 10689.

(20) Yang, X.; Song, X. Q.; Wei, Y.; Wei, W.; Hou, L. X.; Fan, X. J. Synthesis of spinous ZrO_2 core-shell microspheres with good hydrogen storage properties by the pollen bio-template route. *Scr. Mater.* **2011**, *64*, 1075.

(21) Song, B.; Wang, T. T.; Sun, H. G.; Shao, Q.; Zhao, J. K.; Song, K. K.; Hao, L. H.; Wang, L.; Guo, Z. H. Two-step hydrothermally synthesized carbon nanodots/WO_3 photocatalysts with enhanced photocatalytic performance. *Dalton Trans.* **2017**, *46*, 15769.

(22) Dong, W. S.; Lin, F. Q.; Liu, C. L.; Li, M. Y. Synthesis of ZrO_2 nanowires by ionic liquid route. *J. Colloid Interface Sci.* **2009**, *333*, 734.

(23) Li, X.; Ma, G. B.; Liu, Y. Y. Synthesis and Characterization of Magnesium Hydroxide Using a Bubbling Setup. *Ind. Eng. Chem. Res.* **2009**, *48*, 763.

(24) Wu, N. Q.; Wang, J.; Tafen, D. N.; Wang, H.; Zheng, J. G.; Lewis, J. P.; Liu, X. G.; Leonard, S. S.; Manivannan, A. Shape-enhanced photocatalytic activity of single-crystalline anatase TiO_2 (101) nanobelts. *J. Am. Chem. Soc.* **2010**, *132*, 6679.

(25) Hwang, K. J.; Hwang, C. H.; Lee, I. H.; Kim, T.; Jin, S.; Park, J. Y. Synthesis and characterization of hollow metal oxide micro-tubes using a biomaterial template. *Biomass Bioenergy* **2014**, *68*, 62.

(26) Zhang, L.; Yu, W.; Han, C.; Guo, J.; Zhang, Q.; Xie, H.; Shao, Q.; Sun, Z.; Guo, Z. H. Large scaled synthesis of heterostructured electrospun TiO_2/SnO_2 nanofibers with an enhanced photocatalytic activity. *J. Electrochem. Soc.* **2017**, *164*, H651.

(27) Sun, Z.; Zhang, L.; Dang, F.; Liu, Y.; Fei, Z.; Shao, Q.; Lin, H.; Guo, J.; Xiang, L.; Yerra, N.; Guo, Z. H. Experimental and Simulation Understanding of Morphology Controlled Barium Titanate Nanoparticles under Co-adsorption of Surfactants. *CrystEngComm* **2017**, *19*, 3288.

(28) Shao, Q.; Wang, X. J.; Liu, Q. Y.; Wang, L. Y.; Kang, C.; Wang, Q. Y.; Ge, S. S. Preparation and photocatalytic property of porous CuO hollow microspheres via carbon sphere templates. *J. Nanosci. Nanotechnol.* **2011**, *11*, 10271.

(29) Zhu, W. X.; Ge, S. S.; Shao, Q. Adsorption properties of ZrO_2 hollow microboxes prepared using $CaCO_3$ cubes as templates. *RSC Adv.* **2016**, *6*, 81736.

(30) Huang, J.; Wang, X.; Wang, Z. L. Controlled Replication of Butterfly Wings for Achieving Tunable Photonic Properties. *Nano Lett.* **2006**, *6*, 2325.

(31) Rosi, N. L.; Thaxton, C. S.; Mirkin, C. A. Control of nanoparticle assembly by using DNA-modified diatom templates. *Angew. Chem.* **2004**, *116*, 5616.

(32) Li, Y. N.; Su, J.; Lv, X. Y.; Wen, X. Y.; Long, Y. F. Yeast bio-template synthesis of porous anatase TiO_2 and potential application as an anode for sodium-ion batteries. *Electrochim. Acta* **2015**, *182*, 596.

(33) Perry, J. L.; Martin, C. R. Drug-delivery strategies by using template-synthesized nanotubes. Stewart. *Chem. - Eur. J.* **2011**, *17*, 6296.

(34) Bu, D.; Zhuang, H. Synthesis, characterization, and photocatalytic studies of copper-doped TiO_2 hollow spheres using rape pollen as a novel biotemplate. *Catal. Commun.* **2012**, *29*, 24.

(35) Abazari, R.; Mahjoub, A. R. Potential Applications of Magnetic β-$AgVO_3/ZnFe_2O_4$ Nanocomposites in Dyes, Photocatalytic Degradation, and Catalytic Thermal Decomposition of Ammonium Perchlorate. *Ind. Eng. Chem. Res.* **2017**, *56*, 623.

(36) Pan, G. T.; Lai, M. H.; Juang, R. C.; Chung, T. W.; Yang, T. C. K. Preparation of Visible-Light-Driven Silver Vanadates by a Microwave Assisted Hydrothermal Method for the Photodegradation of Volatile Organic Vapors. *Ind. Eng. Chem. Res.* **2011**, *50*, 2807.

(37) Andjelkovic, I.; Stankovic, D.; Nesic, J.; Krstic, J.; Vulic, P.; Manojlovic, D.; Roglic, G. Fe Doped TiO_2 Prepared by Microwave-Assisted Hydrothermal Process for Removal of As(III) and As(V) from Water. *Ind. Eng. Chem. Res.* **2014**, *53*, 10841.

(38) Menon, S. G.; Choudhari, S. G.; Shivashankar, S. A.; Santhosh, C.; Kulkarni, S. D. Thermal effects on rapid microwave synthesized $Co:ZnAl_2O_4$ spinel nanoparticles. *J. Alloys Compd.* **2017**, *728*, 1083.

(39) Wang, C.; Le, Y.; Cheng, B. Fabrication of porous ZrO_2 hollow sphere and its adsorption performance to Congo red in water. *Ceram. Int.* **2014**, *40*, 10847.

(40) Hwang, K. J.; Hwang, C. H.; Lee, I. H.; Kim, T.; Jin, S.; Park, J. Y. Synthesis and characterization of hollow metal oxide micro-tubes using a biomaterial template. *Biomass Bioenergy* **2014**, *68*, 62.

(41) Makkar, P.; Agarwala, R. C.; Agarwala, V. Morphological and Hardness Studies of Electroless Ni-P-ZrO_2 Nanocomposite Coatings on Mild Steel. *Adv. Mater. Res.* **2012**, *585*, 478.

(42) Singhania, A.; Gupta, S. M. Low-temperature CO oxidation over Cu/Pt co-doped ZrO_2 nanoparticles synthesized by solution combustion. *Beilstein J. Nanotechnol.* **2017**, *8*, 264.

(43) Wu, N.; Wei, H.; Zhang, L. Efficient Removal of Heavy Metal Ions with Biopolymer Template Synthesized Mesoporous Titania Beads of Hundreds of Micrometers Size. *Environ. Sci. Technol.* **2012**, *46*, 419.

(44) Topalovic, T.; Nierstrasz, V. A.; Bautista, L.; Jocic, D.; Warmoeskerken, M. M. C. G.; Navarro, A. XPS and contact angle study of cotton surface oxidation by catalytic bleaching. Warmoeskerken. *Colloids Surf., A* **2007**, *296*, 76.

(45) Drăgan, N.; Todan, L.; Voicescu, M.; Răileanu, M.; Crişan, D.; Maganu, M.; Vuluga, D. M.; Ianculescu, A.; Culiţă, D. C. Sol-gel zirconia-based nanopowders with potential applications for sensors. *Ceram. Int.* **2015**, *41*, 4381.

(46) Sevilla, M.; Fuertes, A. B. Catalytic graphitization of templated mesoporous carbons. *Carbon* **2006**, *44*, 468.

(47) Cao, F.; Li, D. X. Morphology-controlled synthesis of SiO_2 hollow microspheres using pollen grain as a biotemplate. *Biomed. Mater.* **2009**, *4*, 025009.

(48) Wang, C.; Wu, Y.; Li, Y.; Shao, Q.; Yan, X.; Han, C.; Wang, Z.; Liu, Z.; Guo, Z. Flame-retardant rigid polyurethane foam with a phosphorus-nitrogen single intumescent flame retardant. *Polym. Adv. Technol.* **2018**, *29*, 668−676.

(49) Fan, X. J.; Song, X. Q.; Yang, X. H.; Hou, L. X. Facile fabrication of ZrO_2 hollow porous microspheres with yeast as bio-templates. *Mater. Res. Bull.* **2011**, *46*, 1315.

(50) Zhao, B. Q.; Shao, Q.; Hao, L. H.; Liu, Z.; Zhang, B.; Ge, S. S.; Zhang, L.; Guo, Z. Yeast-template synthesized Fe-doped cerium oxide hollow microspheres for visible photodegradation of acid orange 7. *J. Colloid Interface Sci.* **2018**, *511*, 39.

(51) Yang, X. H.; Song, X. Q.; Wei, Y.; Wei, W.; Sun, Y. H.; Hou, L. X. Preparation of spinous ZrO_2 microspheres with tunable shell and chamber structure by controlling pollen as a nanoparticles reactor. *J. Nanosci. Nanotechnol.* **2011**, *11*, 10369.

(52) Fazil, A. A.; Bhanu, J. U.; Amutha, A.; Ponpandian, N.; Amirthapandian, S.; Panigrahifacile, B. K.; Thangadurai, P. A facile bio-replicated synthesis of SnO_2 motifs with porous surface by using pollen grains of Peltophorum pterocarpum as a template. *Microporous Mesoporous Mater.* **2015**, *212*, 91.

(53) Thejaswini, T. V. L.; Prabhakaran, d.; Maheswari, M. A. Synthesis of mesoporous worm-like ZrO_2-TiO_2 monoliths and their photocatalytic applications towards organic dye degradation. *J. Photochem. Photobiol., A* **2017**, *344*, 212.

(54) Gu, H.; Rapole, S. B.; Huang, Y.; Cao, D.; Luo, Z.; Wei, S.; Guo, Z. Synergistic interactions between multi-walled carbon nanotubes and toxic hexavalent chromium. *J. Mater. Chem. A* **2013**, *1*, 2011.

(55) Namasivayam, C.; Kavitha, D. Removal of Congo Red from water by adsorption onto activated carbon prepared from coir pith, an agricultural solid waste. *Dyes Pigm.* **2002**, *54*, 47.

(56) Gupta, V. K.; Mittal, A.; Gajbe, V.; Mittal, J. Removal and Recovery of the Hazardous Azo Dye Acid Orange 7 through Adsorption over Waste Materials: Bottom Ash and De-Oiled Soya. *Ind. Eng. Chem. Res.* **2006**, *45*, 1446.

(57) Yu, G. Q.; Lu, Y.; Guo, J.; Patel, M.; Bafana, A.; Wang, X. F.; Qiu, B.; Jeffryes, C.; Wei, S. Y.; Guo, Z. H.; Wujcik, E. K. Carbon nanotubes, graphene, and their derivatives for heavy metal removal. *Adv. Compos. Hybrid Mater.* **2017**, in press, DOI: 10.1007/s42114-017-0004-3.

(58) Gusain, D.; Bux, F.; Sharma, Y. C. Abatement of chromium by adsorption on nanocrystalline zirconia using response surface methodology. *J. Mol. Liq.* **2014**, *197*, 131.